Unexpected anisotropic compression-induced superconductivity in pristine 2H-MoTe$_2$

Tao Lin,[1,*] Run Lv,[2,3,*] Qing Dong,[4,*] Chenyi Li,[1] Bo Liu,[1] Ran Liu,[1] Xiaoling Jing,[1] Yuping Sun [ORCID],[2,5] Quanjun Li,[1,†] Wenjian Lu [ORCID],[2,‡] and Bingbing Liu[1,§]

[1]*State Key Laboratory of Superhard Materials, Jilin University, Changchun 130012, China*
[2]*Key Laboratory of Materials Physics, Institute of Solid State Physics, HFIPS, Chinese Academy of Sciences, Hefei 230031, China*
[3]*Science Island Branch of Graduate School, University of Science and Technology of China, Hefei 230026, China*
[4]*Institute of Applied Physics, Department of Physics and Astronomy, Seoul National University, Seoul 08826, Republic of Korea*
[5]*High Magnetic Field Laboratory, HFIPS, Chinese Academy of Sciences, Hefei 230031, China*

High-pressure application is crucial for shaping material properties and revealing novel phenomena. Materials undergo more unpredictable transitions in their crystal and electronic structures under nonhydrostatic/isotropic pressures than under hydrostatic conditions. However, limited knowledge regarding this behavior exists due to a scarcity of relevant studies. In this study, we systematically investigated the evolution of the structure and electronic states of pristine 2H-MoTe$_2$ in anisotropic pressure environments. Surprisingly, we observed anisotropic compression-induced superconductivity in this material, a phenomenon that is absent in quasihydrostatic environments. High-pressure x-ray diffraction and Raman spectroscopy measurements showed no structural phase transitions; however, an anomalous compressive behavior was observed along the c axis. An anisotropic pressure model was proposed based on experimental conditions. First-principles calculations revealed that a strengthened anisotropic compression effect could enhance electron-phonon coupling by increasing the density of states on the Fermi level and softening the phonon modes, contributing to the emergence of superconductivity in 2H-MoTe$_2$. Our findings offer a route for inducing superconductivity, providing insights into the nature of superconductivity in transition metal dichalcogenides and other similar layered compounds under extreme conditions.

I. INTRODUCTION

High-pressure application is a prominent technique in various scientific disciplines, including materials science, physics, chemistry, and geology, enabling researchers to manipulate crystal structures and discover novel properties in materials [1–4]. In condensed matter physics, pressure modulation can help regulate fundamental physical properties and facilitate qualitative transformations across various material classes, such as insulators, semiconductors, metals, superconductors, ferroelectrics, and topological insulators [5]. Although the application of hydrostatic pressure to materials typically produces isotropic compression [6], maintaining strict hydrostaticity poses challenges due to the solidification of the pressure-transmitting medium (PTM) at high pressures, leading to an anisotropic stress on the materials [7]. Therefore, nonhydrostatic environments are often encountered in high-pressure experiments, leading to complicated compression behaviors in materials [8–11]. Hence, there is a need to improve our understanding of material behavior under compression and provide insights into both isotropic and anisotropic compounds.

Layered materials, characterized by weak van der Waals (vdW) forces between layers, exhibit heightened sensitivity to pressure along the stacking direction, making them particularly susceptible to anisotropic compression effects. For instance, in iron pnictides and heavy fermion superconductors, a less uniform hydrostatic pressure or uniaxial stress often enhances the superconductivity or increases the critical pressure at which superconductivity occurs [12–18]. In transition metal dichalcogenides (TMDCs), nonhydrostatic conditions can induce remarkable phenomena such as isostructural transformation accompanied by metallization and quenchable superconductivity [19,20]. These studies have revealed that the introduction of an anisotropic pressure into the experimental design, particularly uniaxial stress along the stacking direction, holds promise in producing novel physical properties that could aid in the understanding of complex phenomena under extreme pressures and the establishment of new theories.

Among layered compounds, TMDCs stand out for studying anisotropic compression effects owing to their simple structure and diverse physical properties, including semiconducting, semimetallic, and superconducting behaviors, and the formation of charge density waves [21–31]. One representative semiconducting TMDC, 2H-MoTe$_2$ [32,33], exhibits significant pressure sensitivity and undergoes a semiconductor to metal (SM) transition at various critical pressures depending on the pressure environment [34–36]. In this study, we systematically investigated the structural and electronic changes in 2H-MoTe$_2$ under nonhydrostatic pressure conditions and observed unexpected anisotropic compression-induced superconductivity, a phenomenon that is absent in

---

[*]These authors contributed equally to this work.
[†]Contact author: liquanjun@jlu.edu.cn
[‡]Contact author: wjlu@issp.ac.cn
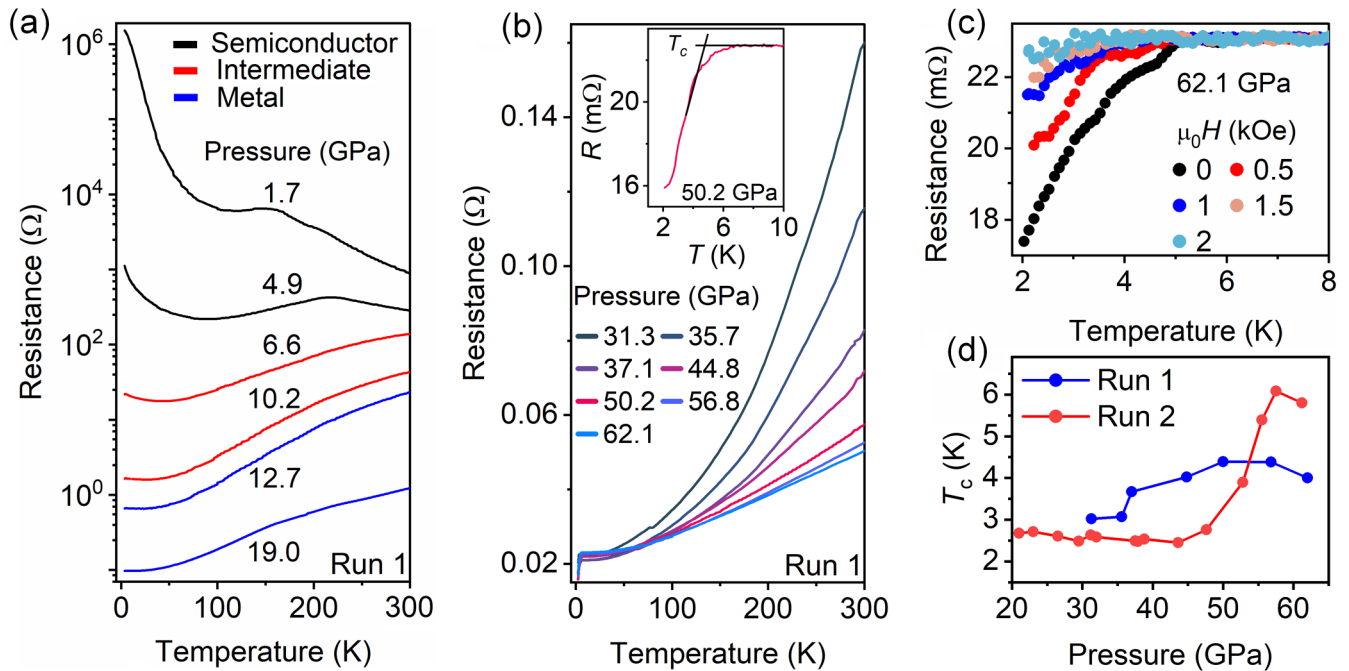[§]Contact author: liubb@jlu.edu.cn

FIG. 1. Temperature-dependent resistance (R-T) curves at selected pressures: (a) 1.7–19.0 GPa and (b) 31.3–62.1 GPa; criterion for determining T_c is shown in (b). (c) R-T curves below 8 K under increasing magnetic fields at 62.1 GPa, and (d) pressure-temperature (P-T_c) phase diagram.

hydrostatic pressure environments. First-principles calculations based on the density functional theory (DFT) [37] have revealed that anisotropic compression promotes electron phonon coupling by increasing the density of states at the Fermi level and softening the phonon modes, thereby contributing to the observed superconductivity.

II. METHODS

Commercially available $2H$-MoTe$_2$ single crystals were used in our experiments. Characterizations were conducted at atmospheric pressure (Fig. S1 in the Supplemental Material [38]); the results helped confirm the high purity and quality of these crystals. High pressures in all the measurements were generated using a diamond anvil cell (DAC) without any PTM to create a nonhydrostatic environment. Pressure calibration can be found in the Supplemental Material [38] (see also Refs. [39,40] therein). Electrical transport measurements were conducted in a nonmagnetic DAC made of a BeCu alloy using the standard four-point probe method in a homemade multifunctional measurement system (2–300 K, Janis Research Company Inc.; 0–9 T, Cryomagnetics Inc.). X-ray diffraction (XRD) measurements were performed at the 4W2 beamline of the Beijing Synchrotron Radiation Facility (BSRF) ($\lambda = 0.6199$ Å). Raman spectra were measured using a micro-Raman system (Renishaw InVia, Renishaw, UK) with a laser at an excitation wavelength of 514.5 nm. Additional details are provided in the Supplemental Material [38].

III. RESULTS AND DISCUSSION

Figure 1 shows the electrical transport measurements. Under ambient conditions, $2H$-MoTe$_2$ behaves as a

semiconductor, and its resistance decreases with increasing temperature because of thermally activated carriers. The temperature-dependent resistance (R-T) curve at an initial pressure of 1.7 GPa confirms the semiconducting state of the sample with a negative dR/dT across the entire temperature range [Fig. 1(a)]. At 6.6 GPa, an SM transition could be observed, with the resistance increasing above 50 K. Figure S4 [38] shows the pressure evolution of the fitted activation energy for the semiconductor state, suggesting a band-gap closure at approximately 6 GPa. However, a residual negative dR/dT persisted at pressures between 6.6 and 12.7 GPa, indicating a partial preservation of the semiconducting state, which is labeled as "intermediate" in Fig. 1(a). At pressures above 12.7 GPa, the metallic state dominated the entire temperature range. Extensive studies have been conducted on the SM transition in $2H$-MoTe$_2$ in both quasihydrostatic and nonhydrostatic environments using various methods. Impedance spectra measurements revealed the SM transition to be at a pressure of $\sim$6 GPa in nonhydrostatic environments, supported by Raman spectra obtained using solid KBr as the PTM [36,41]. These findings were in agreement with our electrical transport measurement results obtained without the PTM. Previous electrical transport measurements in quasihydrostatic environments indicate that metallization begins at 9.6 GPa [34], suggesting a difference of approximately 3 GPa.

Upon further compression, an unexpected phenomenon occurs. At 31.3 GPa, a sudden drop in the resistance was observed below 3 K, indicating the emergence of superconductivity [Fig. 1(b)]. A close-up of the low-temperature range (Fig. S5 [38]) shows that the superconducting transition becomes increasingly evident with increasing pressure. The intersecting lines in the inset of Fig. 1(b) define the

superconducting transition temperature T_c. To validate this unexpected superconductivity, resistance measurements were conducted near T_c under various magnetic fields at 62.1 GPa, as shown in Fig. 1(c). The continuously increasing resistance with increasing magnetic field provides complementary evidence for the superconducting transition in $2H$-MoTe$_2$. The T_c vs H curve plotted in Fig. S6 [38] shows that the upper critical field $[H_{c2}(T)]$ has a positive curvature close to T_c ($H = 0$). Therefore the empirical formula $H_{c2}^*(1-T/T_c)^{1+a}$ was used for fitting and the zero-temperature $\mu_0 H_{c2}(0)$ can be estimated to be 1.3 T at 62.1 GPa. Figure S7 [38] displays the critical field measurements at other pressures. Measurements of the R-T curves in the depressurization process were also conducted, shown in Fig. S8 [38]. It can be found that the superconducting transition fades, and the initial semiconducting state recovers when the pressure is gradually released, revealing the reversible transition in the electronic states. Figure S9 [38] presents the results of the second electrical transport measurement, confirming the nonhydrostatic pressure-induced superconductivity and demonstrating its reproducibility in $2H$-MoTe$_2$. Notably, zero resistance was not reached in both runs, and the resistance drop below T_c is small. Considering that there is no use of PTM in electrical transport measurements, the above phenomena can be attributed to the low superconducting volume, wide transition temperature range, and pressure gradient throughout the sample owing to the nonhydrostatic pressure conditions, which have been observed in several superconducting TMDCs [42–45].

Although previous studies have explored the high-pressure electrical properties of $2H$-MoTe$_2$, there was no observation of its superconductivity in the studies by Zhao *et al.* and Qi *et al.* [34,35]. In Ref. [34], Daphne oil 7373 was used as the PTM to create a quasihydrostatic environment, whereas the PTM used in Ref. [35] was not specified. Our findings suggest that the observed superconductivity is closely related to the nonhydrostatic pressure environment without the use of a PTM. Figure S2 [38] shows the effect of anisotropic compression on $2H$-MoTe$_2$ single crystals within the DAC in our measurements. The sample, resembling a thin flake oriented along the c axis, exhibited a more pronounced compression along the c axis than along the a and b axes, likely facilitating the emergence of superconductivity. Further discussion on the specific mechanism is provided in the theoretical section. Figure 1(d) shows the pressure-temperature (P-T_c) phase diagrams obtained from the two experiments. The superconducting transition could be observed in both experiments, but the variations in T_c differed slightly. Considering that $2H$-MoTe$_2$ superconducts under nonhydrostatic pressure but not under hydrostatic/quasihydrostatic pressure, it can be found that the material is extremely sensitive to the pressure environment. The differences in the experimental setup, sample size, and pressurization procedures of the two runs account for the divergent T_c variations under pressure. Overall, we report the observation of superconductivity in $2H$-MoTe$_2$ under nonhydrostatic conditions, highlighting the extreme sensitivity of this material to pressure environments.

We explored lattice vibrations in $2H$-MoTe$_2$ under the effect of pressure using Raman spectroscopy. Figure S1(b) in the Supplemental Material [38] shows Raman spectra measured at ambient pressure. The observable
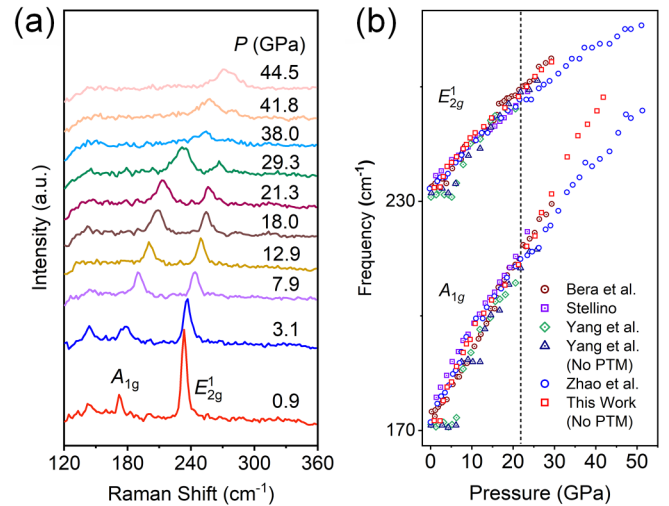

FIG. 2. (a) Raman spectra at various pressures of up to 44.5 GPa; (b) phonon frequencies as a function of the pressure. Raman data obtained from studies conducted by Bera *et al.* [41], Stellino [47], Yang *et al.* [36], and Zhao *et al.* [34] are plotted for comparison.

A_{1g} and E_{2g}^1 modes represent the out of plane vibrations of Te atoms and in-plane vibrations of Mo and Te atoms, respectively [46]. Fig. 2 shows the high-pressure Raman spectra at pressures of up to 44.5 GPa. With increasing pressure, both modes shift toward higher frequencies owing to the compacted lattice, accompanied by a visible broadening of the peaks owing to the shortened phonon lifetime upon compression [47]. The intensity of the E_{2g}^1 mode decreases as pressure increases, and the E_{2g}^1 mode finally disappears at pressures above 29.3 GPa. However, the A_{1g} mode does not disappear at 29.3 GPa but remains stable up to 44.5 GPa. Figures 2(b) and S10(a) [38] show the pressure-dependent phonon frequencies of the two modes. Above 12.9 GPa, the slight changes in the pressure coefficients (Fig. S10(a) [38]) align with the critical pressure of metallization observed in the electrical transport measurements. A further analysis of the relative intensity ratios (Fig. S10(b) [38]) reveals discontinuities at pressures of approximately 6.3 and 12.9 GPa, corresponding to the SM transition process. For comparison, previous Raman data obtained using the PTM and our results are plotted in Fig. 2(b). Above 21.3 GPa, a noticeable difference was observed. The A_{1g} mode (out of plane vibration) in our measurement exhibited faster compressive behavior, revealing strengthened interlayer interactions in nonhydrostatic environments in higher pressure ranges.

High-pressure synchrotron XRD measurements were conducted to investigate the structural evolution of $2H$-MoTe$_2$ and its impact on electronic states. Details of XRD data processing can be found in the Supplemental Material [38] (see also Refs. [48,49] therein). Figure 3(a) shows the XRD patterns at representative pressures of up to 54.0 GPa. A Rietveld refinement at 1.6 GPa revealed that the sample corresponded well to the $P6_3/mmc$ structure (2H). With increasing pressure, all the peaks shifted to higher angles. No new peaks emerged during continuous compression, suggesting the absence of a structural phase transition. The XRD patterns in
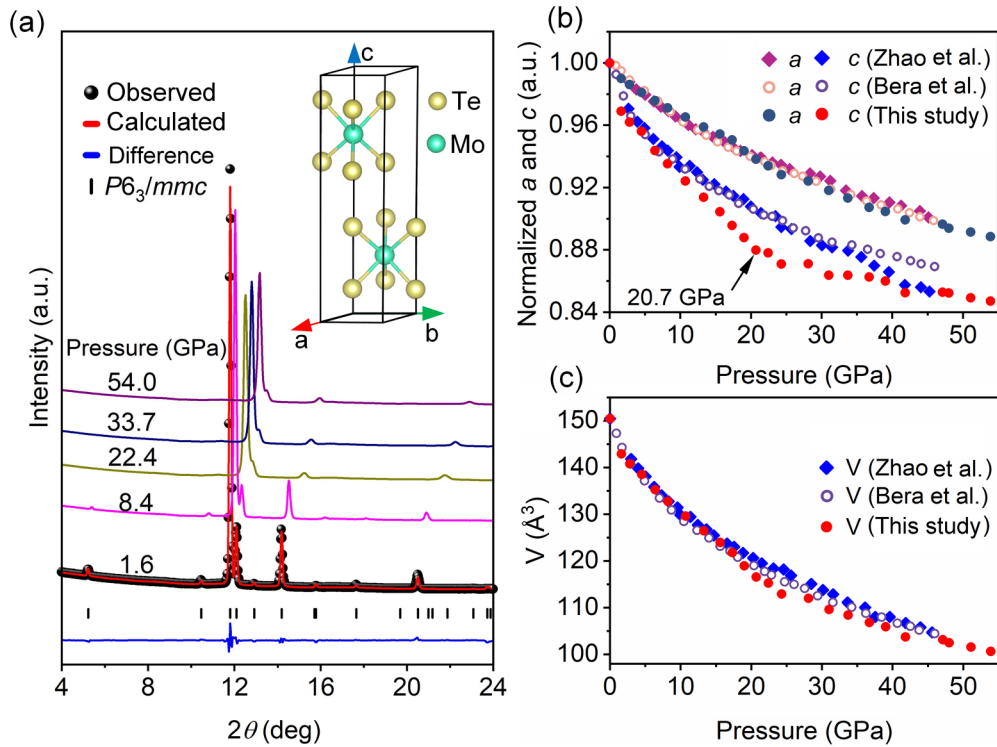
FIG. 3. (a) Synchrotron XRD patterns of $2H$-MoTe$_2$ at selected pressures of up to 54.0 GPa. The bottom panel shows the Rietveld refinement using the $P6_3/mmc$ structure. The inset shows the schematic of a $2H$-MoTe$_2$ unit cell. Pressure dependencies of (b) normalized lattice constants and (c) cell volume. The reference data points obtained from the study by Zhao *et al.* (PTM: silicon oil) [34] and Bera *et al.* (PTM: Ne) [50] are plotted for comparison.

the depressurization process are depicted in Fig. S11 [38], which show a reversible change compared to the pressure increase process. As pressure decreased, all diffraction peaks shifted toward lower angles without the appearance of new peaks. Figures 3(b) and 3(c) show the pressure dependencies of the lattice constants a and c and volume V, obtained from the refinements. For comparison, the referenced experimental XRD data using PTM [34,50] were also included. Below 20.7 GPa, the compressive behavior was faster in the c axis than in the a axis, indicating a typical anisotropic compression effect that is prevalent in layered TMDCs owing to the weak interlayer vdW bonds [51–54]. However, above ~20.7 GPa, the compressibility in the c axis was similar to that in the a axis, attributed to strengthened interlayer interactions. In addition, the lattice constants a and c and volume V continued to decrease. These results demonstrated that the $2H$ structure maintains high stability in nonhydrostatic pressure environments, consistent with the results of previous high-pressure studies using PTM.

Although no structural phase transition occurred, the pressure-induced evolution of the structural parameters in the various pressure environments remained distinct. In our measurement, the c-axis compressibility decreased almost linearly until a pressure of 20.7 GPa, while in quasihydrostatic [34] or hydrostatic [50] environments, it is known to decrease smoothly across the entire pressure range, revealing a more significant compressibility rate along the c axis in nonhydrostatic environments. Figure S12 [38] shows the pressure dependence of the c/a ratio, including our measurements and those obtained from previous studies, indicating a

more pronounced anisotropic compression in nonhydrostatic environments. By analyzing the changes in the compressibility rate, we fitted the pressure-dependent volume curve [55] to two sections before and after a pressure of 20.7 GPa, which is shown in Fig. S13 in the Supplemental Material [38]. The subsequently obtained bulk moduli were 92.1 ± 4.0 and 103.4 ± 7.7 GPa in the low- and high-pressure ranges, respectively, indicating that $2H$-MoTe$_2$ is highly compressible above 20.7 GPa in nonhydrostatic environments. These results reveal that under nonhydrostatic pressure conditions, $2H$-MoTe$_2$ is subjected to a more significant stress along the c axis, demonstrating the strong effect of anisotropic compression in our case.

The electrical, Raman, and XRD measurement results evidently showed that $2H$-MoTe$_2$ exhibits an advanced SM transition pressure, undiscovered superconductivity, stable structure, and significant anisotropic compression effects under nonhydrostatic pressure conditions. To understand the intrinsic underlying mechanisms, we performed first-principles calculations based on density-functional theory (DFT), as detailed in the Supplemental Material [38] (see also Refs. [37,56–61] therein). Based on the high compressibility rate along the c axis observed from the XRD results, we proposed an anisotropic pressure model. In this model, the anisotropic parameter n is defined by the formula $n = P_c/P_{a=b}$, where P_c represents the pressure parallel to the c axis and $P_{a=b}$ is parallel to the ab face. $n = 1$ indicates a perfectly isotropic condition. When $n > 1$, an anisotropic compression effect appeared that became stronger with increasing n. Our calculations relied on a given n under varying P_c.
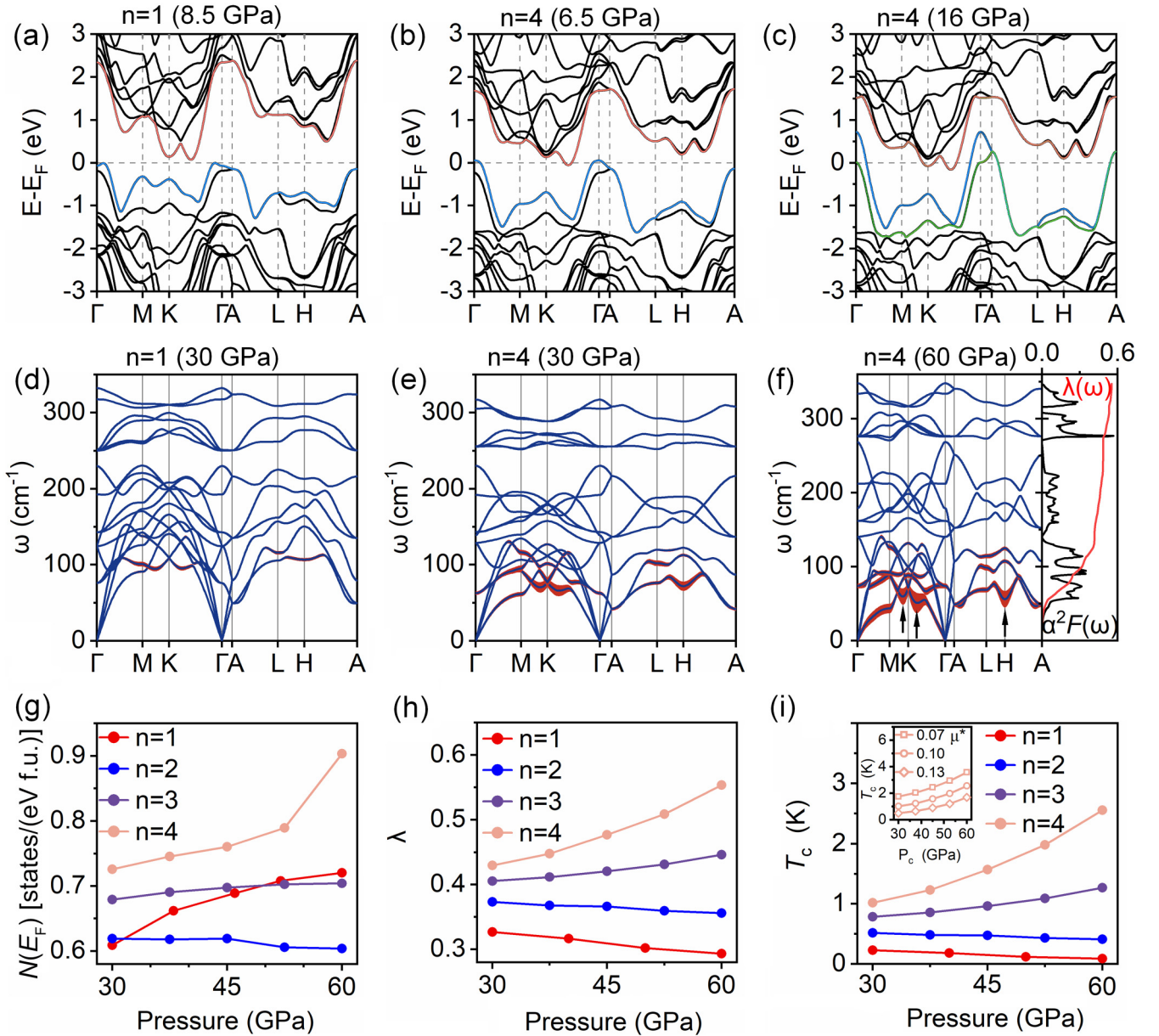
FIG. 4. Theoretical calculations under different pressures (P_c) and anisotropic parameters (n). (a)–(c) Band structures with SOC for various n and P_c. (d)–(f) Phonon dispersions with EPC constants λ_{qv} depicted by red shadows under different n and P_c. The red shadows highlight the phonon branches that contribute significantly to the EPC constant. The right side of (f) shows the Eliashberg function $\alpha^2 F(\omega)$ and integrated EPC strength $\lambda(\omega)$. Pressure evolutions of (g) density of states $N(E_F)$ at the Fermi level and (h) EPC constants λ. The Coulomb pseudopotential μ^* is set to a typical value of 0.1 [61]. (i) Calculated T_c as a function of the pressure for $n = 1, 2, 3$, and 4; the inset shows the variation in T_c at different Coulomb pseudopotential μ^* values for $n = 4$.

We first explored the relationship between the SM transition pressure and anisotropic parameter n. Figure S14 [38] shows the band structure of $2H$-MoTe$_2$ at ambient pressure, revealing an indirect band gap. Figures 4(a)–4(c) show the band structures with spin-orbit coupling (SOC) at different pressures for various n. The critical pressure for the SM transition under isotropic conditions ($n = 1$) was calculated to be 8.5 GPa [Fig. 4(a)]. For $n > 1$, and as n increased, which is indicative of a strengthening anisotropic compression effect, the SM transition pressure gradually decreased. For instance, when n was fixed at 4, the SM transition pressure was calculated to be 6.5 GPa, which matched our

experimentally observed value. This consistency suggests the presence of strong anisotropic compression effects in our experiments, which contributed to the advancement of the SM transition point. In addition, we identified the previously reported Lifshitz transition [41,62], which is discussed in detail in Fig. S15 in the Supplemental Material [38].

Next, we calculated the electron-phonon coupling (EPC), phonon dispersion, Eliashberg spectral function $\alpha^2 F(\omega)$, and electron-phonon integral $\lambda(\omega)$ at higher P_c and various n. Under 30 GPa, $2H$-MoTe$_2$ exhibited EPC regardless of whether $n = 1$ or 4, resulting in certain superconducting transition temperatures. However, the EPC was stronger under strong

anisotropic compression ($n = 4$) than under isotropic conditions ($n = 1$), as indicated by the red shadows in Figs. 4(d) and 4(e). To further understand the evolution of superconductivity with increasing anisotropy, we calculated the changes in the density of states $N(E_F)$, EPC strength λ, and T_c as a function of the pressure for $n = 1$, 2, 3, and 4, respectively. Figures 4(g)–4(i) show the results. Under hydrostatic conditions ($n = 1$), the calculated T_c was less than 0.1 K, and it decreased with increasing pressure. However, it is challenging to achieve this extremely low temperature. Therefore, no superconductivity was detected in previous hydrostatic measurements. For $n > 1$, and as n increased, the calculated T_c increased substantially, suggesting that the enhanced anisotropic compression significantly improved the superconductivity. Figure 4(i) and its inset show that the calculated T_c for $n = 4$ closely matches the measured value. Moreover, the increasing trend in the calculated T_c with pressure is also consistent with the T_c-P phase diagram shown in Fig. 1(d). This reveals that the strong anisotropic compression for $n = 4$ approximately aligns with the experimental conditions. Returning to Figs. 4(d)–4(h), it can be seen that the increased T_c for $n = 4$ may be primarily attributed to the increase in the EPC constant λ, which correlates with increasing $N(E_F)$ and softening of the phonon modes under pressure. The three arrows in Fig. 4(f) indicate the softening modes that predominantly contributed to the EPC. Overall, an increase in the pressure and its anisotropy enhanced the density of states on the Fermi level and further softened the phonon modes, contributing to the increased EPC strength and resulting in improved superconductivity in $2H$-MoTe$_2$. The excellent agreement between the theoretical calculations and experimental results indicated that layered materials can exhibit unexpectedly excellent properties under nonhydrostatic pressures and that anisotropic compressibility contributes to the emergence of exotic phenomena, providing a different perspective for high-pressure superconductivity research.

IV. SUMMARY

In conclusion, we observed an unexpected anisotropic compression-induced superconductivity in semiconducting $2H$-MoTe$_2$ under a nonhydrostatic pressure condition. Although no structural phase transition occurred, we report a pronounced anisotropic compressive behavior of the lattice constants in nonhydrostatic environments, unlike that observed under hydrostatic or quasihydrostatic conditions. Theoretical calculations provide further support for the emergence of superconductivity in $2H$-MoTe$_2$, with increased EPC constants resulting from anisotropic compression. These findings have significant implications for understanding the nature of superconductivity in TMDCs and similar layered systems under extreme conditions. Moreover, they offer a fresh perspective for inducing unexpected properties in materials.

[1] A. Jayaraman, Diamond anvil cell and high-pressure physical investigations, Rev. Mod. Phys. **55**, 65 (1983).

[2] R. J. Hemley, Effects of high pressure on molecules, Annu. Rev. Phys. Chem. **51**, 763 (2000).

[3] P. F. McMillan, New materials from high-pressure experiments, Nat. Mater. **1**, 19 (2002).

[4] M. Miao, Y. Sun, E. Zurek, and H. Lin, Chemistry under high pressure, Nat. Rev. Chem. **4**, 508 (2020).

[5] H.-K. Mao, B. Chen, J. Chen, K. Li, J.-F. Lin, W. Yang, and H. Zheng, Recent advances in high-pressure science and technology, Matter Radiat. Extremes **1**, 59 (2016).

[6] K. Takemura, Hydrostatic experiments up to ultrahigh pressures, J. Phys. Soc. Jpn. **76**, 202 (2007).

[7] S. Klotz, J. C. Chervin, P. Munsch, and G. Le Marchand, Hydrostatic limits of 11 pressure transmitting media, J. Phys. D: Appl. Phys. **42**, 075413 (2009).

[8] C. Liu, X. Song, Q. Li, Y. Ma, and C. Chen, Smooth flow in diamond: Atomistic ductility and electronic conductivity, Phys. Rev. Lett. **123**, 195504 (2019).

[9] C. Liu, X. Song, Q. Li, Y. Ma, and C. Chen, Superconductivity in compression-shear deformed diamond, Phys. Rev. Lett. **124**, 147001 (2020).

[10] X. Song, C. Liu, Q. Li, R. J. Hemley, Y. Ma, and C. Chen, Stress-induced high-T_c superconductivity in solid molecular hydrogen, Proc. Natl. Acad. Sci. USA **119**, e2122691119 (2022).

[11] K. Matsubayashi, T. Terai, J. S. Zhou, and Y. Uwatoko, Superconductivity in the topological insulator Bi$_2$Te$_3$ under hydrostatic pressure, Phys. Rev. B **90**, 125126 (2014).

[12] N. J. Hillier, N. Foroozani, D. A. Zocco, J. J. Hamlin, R. E. Baumbach, I. K. Lum, M. B. Maple, and J. S. Schilling, Intrinsic dependence of T_c on hydrostatic (He-gas) pressure for superconducting LaFePO, PrFePO, and NdFePO single crystals, Phys. Rev. B **86**, 214517 (2012).

[13] E. Gati, L. Xiang, S. L. Bud'ko, and P. C. Canfield, Hydrostatic and uniaxial pressure tuning of iron-based superconductors: insights into superconductivity, magnetism, nematicity, and collapsed tetragonal transitions, Ann. Phys. **532**, 2000248 (2020).

[14] H. Kotegawa, T. Kawazoe, H. Sugawara, K. Murata, and H. Tou, Effect of uniaxial stress for pressure-induced superconductor SrFe$_2$As$_2$, J. Phys. Soc. Jpn. **78**, 083702 (2009).

[15] T. Yamazaki, N. Takeshita, R. Kobayashi, H. Fukazawa, Y. Kohori, K. Kihou, C. H. Lee, H. Kito, A. Iyo, and H. Eisaki, Appearance of pressure-induced superconductivity in BaFe$_2$As$_2$ under hydrostatic conditions and its extremely high sensitivity to uniaxial stress, Phys. Rev. B **81**, 224511 (2010).

[16] W. Yu, A. A. Aczel, T. J. Williams, S. L. Bud'ko, N. Ni, P. C. Canfield, and G. M. Luke, Absence of superconductivity in single-phase CaFe$_2$As$_2$ under hydrostatic pressure, Phys. Rev. B **79**, 020511(R) (2009).

[17] C. Yang, J. Guo, S. Cai, Y. Zhou, V. A. Sidorov, C. Huang, S. Long, Y. Shi, Q. Chen, S. Tan, Q. Wu, P. Coleman, T. Xiang, and L. Sun, Quasi-uniaxial pressure induced superconductivity in the stoichiometric compound UTe_2, Phys. Rev. B **106**, 024503 (2022).

[18] N. Oeschler, P. Gegenwart, M. Lang, R. Movshovich, J. L. Sarrao, J. D. Thompson, and F. Steglich, Uniaxial pressure effects on $CeIrIn_5$ and $CeCoIn_5$ studied by low-temperature thermal expansion, Phys. Rev. Lett. **91**, 076402 (2003).

[19] S. Duwal and C.-S. Yoo, Shear-induced isostructural phase transition and metallization of layered tungsten disulfide under nonhydrostatic compression, J. Phys. Chem. C **120**, 5101 (2016).

[20] U. Dutta, P. S. Malavi, S. Sahoo, B. Joseph, and S. Karmakar, Pressure-induced superconductivity in semimetallic $1T$-$TiTe_2$ and its persistence upon decompression, Phys. Rev. B **97**, 060503(R) (2018).

[21] R. V. Kasowski, Band structure of MoS_2 and NbS_2, Phys. Rev. Lett. **30**, 1175 (1973).

[22] C. B. Scruby, P. M. Williams, and G. S. Parry, The role of charge density waves in structural transformations of $1T$ TaS_2, Philos. Mag. **31**, 255 (1975).

[23] T. F. Smith, R. N. Shelton, and R. E. Schwall, Superconductivity of $TaS_{2-x}Se_x$ layer compounds at high pressure, J. Phys. F: Met. Phys. **5**, 1713 (1975).

[24] R. Z. Bachrach, M. Skibowski, and F. C. Brown, Angle-resolved photoemission from $TiSe_2$ using synchrotron radiation, Phys. Rev. Lett. **37**, 40 (1976).

[25] D. E. Moncton, J. D. Axe, and F. J. DiSalvo, Neutron scattering study of the charge-density wave transitions in $2H$-$TaSe_2$ and $2H$-$NbSe_2$, Phys. Rev. B **16**, 801 (1977).

[26] J. Augustin, V. Eyert, T. Böker, W. Frentrup, H. Dwelk, C. Janowitz, and R. Manzke, Electronic band structure of the layered compound Td-WTe_2, Phys. Rev. B **62**, 10812 (2000).

[27] A. Klein, S. Tiefenbacher, V. Eyert, C. Pettenkofer, and W. Jaegermann, Electronic band structure of single-crystal and single-layer WS_2: Influence of interlayer van der Waals interactions, Phys. Rev. B **64**, 205416 (2001).

[28] I. Guillamón, H. Suderow, S. Vieira, L. Cario, P. Diener, and P. Rodière, Superconducting density of states and vortex cores of $2H$-NbS_2, Phys. Rev. Lett. **101**, 166407 (2008).

[29] Y. Sun, S.-C. Wu, M. N. Ali, C. Felser, and B. Yan, Prediction of Weyl semimetal in orthorhombic $MoTe_2$, Phys. Rev. B **92**, 161107(R) (2015).

[30] Y. Fang, J. Pan, J. He, R. Luo, D. Wang, X. Che, K. Bu, W. Zhao, P. Liu, G. Mu, H. Zhang, T. Lin, and F. Huang, Structure Re-determination and superconductivity observation of bulk $1T$ MoS_2, Angew. Chem. **57**, 1232 (2018).

[31] Y. Fang, J. Pan, D. Zhang, D. Wang, H. T. Hirose, T. Terashima, S. Uji, Y. Yuan, W. Li, Z. Tian, J. Xue, Y. Ma, W. Zhao, Q. Xue, G. Mu, H. Zhang, and F. Huang, Discovery of superconductivity in $2M$ WS_2 with possible topological surface states, Adv. Mater. **31**, 1901942 (2019).

[32] I. G. Lezama, A. Arora, A. Ubaldini, C. Barreteau, E. Giannini, M. Potemski, and A. F. Morpurgo, Indirect-to-direct band gap crossover in few-layer $MoTe_2$, Nano Lett. **15**, 2336 (2015).

[33] Y.-F. Lin, Y. Xu, S.-T. Wang, S.-L. Li, M. Yamamoto, A. Aparecido-Ferreira, W. Li, H. Sun, S. Nakaharai, W.-B. Jian, K. Ueno, and K. Tsukagoshi, Ambipolar $MoTe_2$ transistors and their applications in logic circuits, Adv. Mater. **26**, 3263 (2014).

[34] X. M. Zhao, H. Y. Liu, A. F. Goncharov, Z.-W. Zhao, V. V. Struzhkin, H.-K. Mao, A. G. Gavriliuk, and X.-J. Chen, Pressure effect on the electronic, structural, and vibrational properties of layered $2H$-$MoTe_2$, Phys. Rev. B **99**, 024111 (2019).

[35] Y. Qi, P. G. Naumov, M. N. Ali, C. R. Rajamathi, W. Schnelle, O. Barkalov, M. Hanfland, S.-C. Wu, C. Shekhar, Y. Sun, V. Süß, M. Schmidt, U. Schwarz, E. Pippel, P. Werner, R. Hillebrand, T. Förster, E. Kampert, S. Parkin, R. J. Cava *et al.*, Superconductivity in Weyl semimetal candidate $MoTe_2$, Nat. Commun. **7**, 11038 (2016).

[36] L. Yang, L. Dai, H. Li, H. Hu, K. Liu, C. Pu, M. Hong, and P. Liu, Characterization of the pressure-induced phase transition of metallization for $MoTe_2$ under hydrostatic and non-hydrostatic conditions, AIP Adv. **9**, 065104 (2019).

[37] G. Kresse and J. Hafner, *Ab initio* molecular dynamics for liquid metals, Phys. Rev. B **47**, 558 (1993).

[38] See Supplemental Material at http://link.aps.org/supplemental/10.1103/PhysRevB.110.104511 for additional information about the experimental methods, calculation details, and supplemental figures, which includes Refs. [34,37,39,40,46,48,49,55–62].

[39] H. K. Mao, J. Xu, and P. M. Bell, Calibration of the ruby pressure gauge to 800 kbar under quasi-hydrostatic conditions, J. Geophys. Res.: Solid Earth **91**, 4673 (1986).

[40] Y. Akahama and H. Kawamura, Pressure calibration of diamond anvil Raman gauge to 310 GPa, J. Appl. Phys. **100**, 043516 (2006).

[41] A. Bera, A. Singh, D. V. S. Muthu, U. V. Waghmare, and A. K. Sood, Pressure-dependent semiconductor to semimetal and Lifshitz transitions in $2H$-$MoTe_2$: Raman and first-principles studies, J. Phys.: Condens. Matter **29**, 105403 (2017).

[42] C. Tian, Y. Gao, F. Tian, X. Wang, Z. Zhang, D. Duan, X. Huang, and T. Cui, Dimensionality switching and superconductivity transition in dense $1T$-$HfSe_2$, Phys. Rev. B **105**, L180506 (2022).

[43] Z. Chi, X. Chen, F. Yen, F. Peng, Y. Zhou, J. Zhu, Y. Zhang, X. Liu, C. Lin, S. Chu, Y. Li, J. Zhao, T. Kagayama, Y. Ma, and Z. Yang, Superconductivity in pristine $2H_a$-MoS_2 at ultrahigh pressure, Phys. Rev. Lett. **120**, 037002 (2018).

[44] D. Zhou, Y. Zhou, C. Pu, X. Chen, P. Lu, X. Wang, C. An, Y. Zhou, F. Miao, C.-H. Ho, J. Sun, Z. Yang, and D. Xing, Pressure-induced metallization and superconducting phase in ReS_2, npj Quantum Mater. **2**, 19 (2017).

[45] Q. Dong, J. Pan, S. Li, Y. Fang, T. Lin, S. Liu, B. Liu, Q. Li, F. Huang, and B. Liu, Record-high superconductivity in transition metal dichalcogenides emerged in compressed $2H$-TaS_2, Adv. Mater. **34**, 2103168 (2022).

[46] S. Caramazza, A. Collina, E. Stellino, F. Ripanti, P. Dore, and P. Postorino, First- and second-order Raman scattering from $MoTe_2$ single crystal, Eur. Phys. J. B **91**, 35 (2018).

[47] E. Stellino, Pressure evolution of the optical phonons of $MoTe_2$, Nuovo Cim. C **43**, 116 (2020).

[48] C. Prescher and V. B. Prakapenka, DIOPTAS: A program for reduction of two-dimensional x-ray diffraction data and data exploration, High Pressure Res. **35**, 223 (2015).

[49] B. H. Toby and R. B. Von Dreele, GSAS-II: The genesis of a modern open-source all purpose crystallography software package, J. Appl. Crystallogr. **46**, 544 (2013).

[50] A. Bera, A. Singh, S. N. Gupta, K. Glazyrin, D. V. S. Muthu, U. V. Waghmare, and A. K. Sood, Pressure-induced isostructural electronic topological transitions in $2H$-MoTe$_2$: X-ray diffraction and first-principles study, J. Phys.: Condens. Matter **33**, 065402 (2021).

[51] X. Wang, X. Chen, Y. Zhou, C. Park, C. An, Y. Zhou, R. Zhang, C. Gu, W. Yang, and Z. Yang, Pressure-induced iso-structural phase transition and metallization in WSe$_2$, Sci. Rep. **7**, 46694 (2017).

[52] Z. Zhao, H. Zhang, H. Yuan, S. Wang, Y. Lin, Q. Zeng, G. Xu, Z. Liu, G. K. Solanki, K. D. Patel, Y. Cui, H. Y. Hwang, and W. L. Mao, Pressure induced metallization with absence of structural transition in layered molybdenum diselenide, Nat. Commun. **6**, 7312 (2015).

[53] A. P. Nayak, Z. Yuan, B. Cao, J. Liu, J. Wu, S. T. Moran, T. Li, D. Akinwande, C. Jin, and J.-F. Lin, Pressure-modulated conductivity, carrier density, and mobility of multilayered tungsten disulfide, ACS Nano **9**, 9117 (2015).

[54] Z.-H. Chi, X.-M. Zhao, H. Zhang, A. F. Goncharov, S. S. Lobanov, T. Kagayama, M. Sakata, and X.-J. Chen, Pressure-induced metallization of molybdenum disulfide, Phys. Rev. Lett. **113**, 036802 (2014).

[55] F. Birch, Finite elastic strain of cubic crystals, Phys. Rev. **71**, 809 (1947).

[56] A. Kokalj, Computer graphics and graphical user interfaces as tools in simulations of matter at the atomic scale, Comput. Mater. Sci. **28**, 155 (2003).

[57] S. Grimme, S. Ehrlich, and L. Goerigk, Effect of the damping function in dispersion corrected density functional theory, J. Comput. Chem. **32**, 1456 (2011).

[58] P. Giannozzi, S. Baroni, N. Bonini, M. Calandra, R. Car, C. Cavazzoni, D. Ceresoli, G. L. Chiarotti, M. Cococcioni, I. Dabo *et al.*, QUANTUM ESPRESSO: A modular and open-source software project for quantum simulations of materials, J. Phys.: Condens. Matter **21**, 395502 (2009).

[59] P. B. Allen and R. C. Dynes, Transition temperature of strong-coupled superconductors reanalyzed, Phys. Rev. B **12**, 905 (1975).

[60] P. Morel and P. W. Anderson, Calculation of the superconducting state parameters with retarded electron-phonon interaction, Phys. Rev. **125**, 1263 (1962).

[61] M. Calandra and F. Mauri, Charge-density wave and superconducting dome in TiSe$_2$ from electron-phonon interaction, Phys. Rev. Lett. **106**, 196406 (2011).

[62] I. M. Lifshitz, Anomalies of electron characteristics of a metal in the high pressure region, Sov. Phys. JETP **11**, 1130 (1960).